Supplemental Information for:

Lattice-engineered asymmetric Mn-O-Ru motifs with bridge oxygen vacancies for efficient acidic water oxidation

1 Experimental section

Pretreatment of Carbon Cloth

The carbon cloth was cut into an appropriate size, immersed in a mixed acid solution of concentrated nitric acid and concentrated sulfuric acid at a volume ratio of 3:1, and sonicated for 1 h. The carbon cloth was then taken out and rinsed with deionized water, followed by ultrasonication in acetone for 10 min. After retrieval, the carbon cloth was rinsed again with deionized water and subsequently sonicated in deionized water and anhydrous ethanol successively for 10 min each. This cycle was repeated three times to complete the pretreatment of the carbon cloth.

Synthesis of MnO_2 support

Linear α-MnO_2 (MnO_2 NW) and flaky α-MnO_2 (MnO_2 NS) were synthesized via a typical hydrothermal method. Preparation of MnO_2 NW: 0.1 mmol of $KMnO_4$ and 2.35 mmol of K_2SO_4 were dissolved in 35 mL of deionized water, followed by the dropwise addition of 0.5 mL of concentrated H_2SO_4 (98%). The mixture was magnetically stirred for 30 min to achieve thorough mixing. Subsequently, the mixture, together with the pretreated carbon cloth, was transferred into a Teflon-lined stainless-steel autoclave and reacted at 120 °C for 90 min. After cooling down, the carbon cloth was taken out, rinsed repeatedly with deionized water and anhydrous ethanol, and then dried in a vacuum oven at 60 °C for 2 h. The MnO_2 NS sample was prepared by adopting the identical procedure to that for MnO_2 NW, except for the use of different reactant ratios (0.8 mmol of $KMnO_4$ and 2 mmol of K_2SO_4). The MnO_2 nanoneedles sample was prepared by adopting the identical procedure to that for MnO_2 NW, except for the use of different reactant ratios (0.4 mmol of $KMnO_4$ and 2.2 mmol of K_2SO_4).

Synthesis of Ru-MnO_2 catalyst

The dried carbon cloth was immersed in a 4.82 mmol L^{-1} $RuCl_3$ solution and subjected to ion exchange at 60 °C for 10 h. After cooling, the carbon cloth was taken out, rinsed repeatedly with deionized water and anhydrous ethanol, and then dried in a vacuum oven at 60 °C for 2 h. Finally, the dried carbon cloth was placed in a clean porcelain boat and calcined at 200 °C for 5 h under a N_2 atmosphere in a tube furnace to obtain Ru-MnO_2 NW. The synthesis process of Ru-MnO_2 NS was the same as that of Ru-MnO_2 NW.

Prepared of commercial RuO_2 electrode

1 mg of RuO_2 was dissolved in a mixed solution containing 250 μL of anhydrous ethanol, 700 μL of deionized water and 50 μL of Nafion solution (0.5 wt%). The above solution was drop-cast onto a 1 cm × 1 cm carbon paper in several batches and dried repeatedly to prepare a RuO_2 working electrode with a loading of 1 mg cm^{-2} for the OER test.

Structural Characterization

The crystallographic information of the materials was acquired by powder X-ray diffraction (XRD, Rigaku Smartlab with Cu Kα radiation). X-ray photoelectron spectroscopy (XPS) analysis was performed on Thermo Scientific ESCALAB 250Xi (Al Kα 1486.6 eV) and the binding energy was calibrated with C 1s at 284.8 eV. Elemental analysis was detected by NexION 2000 inductively coupled plasma-atomic emission spectrometry (ICP-OES). Elemental analysis was detected by NexION 2000 inductively coupled plasma-atomic emission spectrometry (ICP-OES). Field-emission transmission electron microscopy (TEM) and energy-dispersive X-ray spectroscopy (EDS) measurements were carried out on a JEOL JEM-F200 instrument (Japan). Scanning electron microscopy (SEM) characterization was performed using a ZEISS Sigma 300 microscope (Germany). High-angle annular dark-field scanning transmission electron microscopy (HAADF-STEM) observations were conducted on the JEM-F200 microscope operated at 200 kV.

Electrochemical measurements

Electrochemical measurements of all samples were performed on a CHI 760E electrochemical workstation with 0.5 M H_2SO_4 as the electrolyte. All the tests were conducted at room temperature unless otherwise specified. A standard three-electrode system was employed, using 1 cm × 1 cm samples. An Ag/AgCl electrode served as the reference electrode, a platinum mesh as the counter electrode, and the catalyst immobilized by a platinum plate electrode holder as the working electrode. A magnetic stir bar was placed in the electrolytic cell to facilitate rapid removal of generated bubbles. The measured potential was iR-compensated and converted to the reversible hydrogen electrode (RHE) scale using the equation: E (vs. RHE) = E (vs. Ag/AgCl) + 0.198V + 0.0591×PH – iR, where i is the current and R is the uncompensated resistance. Prior to the formal measurements, the catalysts were subjected to hundreds of cyclic voltammetry (CV) cycles to achieve a steady state. Linear sweep voltammetry (LSV) curves were recorded by scanning the potential from high to low values at a scan rate of 10 mV s^{-1}. Electrochemical impedance spectroscopy (EIS) measurements were carried out at 1.4 V over a frequency range from 0.01 Hz to 100 kHz, and the results were presented as Nyquist plots. The electrochemical surface area (ECSA) was calculated from the double-layer capacitance C_{dl} using the formula: ECSA = C_{dl} / C_s, where C_s is the specific capacitance of a flat surface (0.035 mF cm^{-2}). The C_{dl} values were obtained from CV measurements performed in the non-faradaic potential region (1.0-1.1V) at various scan rates (10, 20, 30, 40, 50, 60 and 70 mV s^{-1}). The stability of the catalysts was evaluated by comparing the potential difference required to reach a current density of 10 mA cm^{-2} before and after 5000 CV cycles, and a chronopotentiometry test was also conducted at a constant current density of 10 mA cm^{-2} for 920 h.

Mass activity and TOF calculations

The mass activity (A g_{Ru}^{-1}) was calculated based on the Ru metal loading (m_{Ru})

and current density (j) at the potential of 1.3V and 1.6V:

$$Mass\ activity\ = \frac{j}{m_{Ru}}$$

The TOF was calculated based on the number of active sites and j as follows:

$$TOF\ (s^{-1}) = \frac{j * M_{Ru}}{n * F * m_{Ru}}$$

2 Supplementary figures

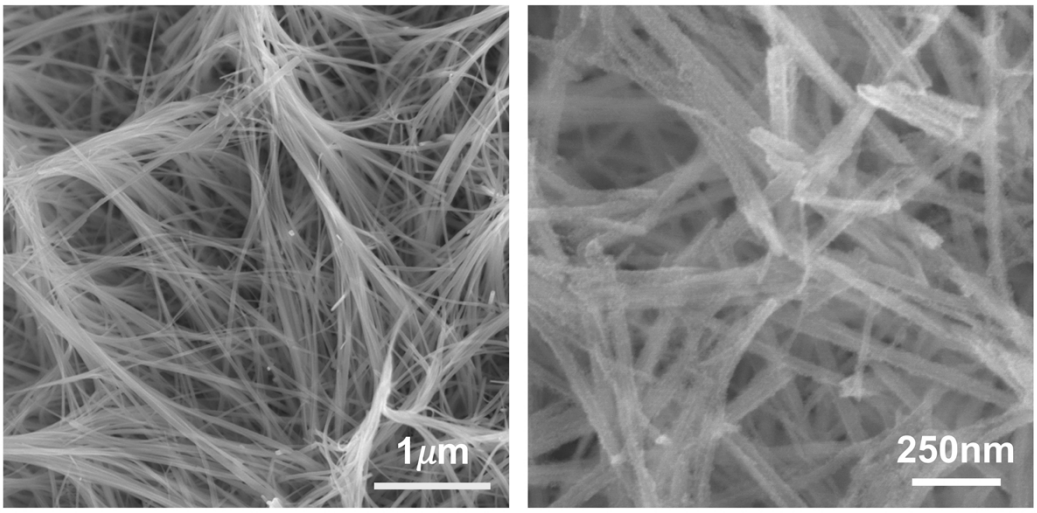

Figure S1. SEM images of α-MnO_2 nanowires obtained.

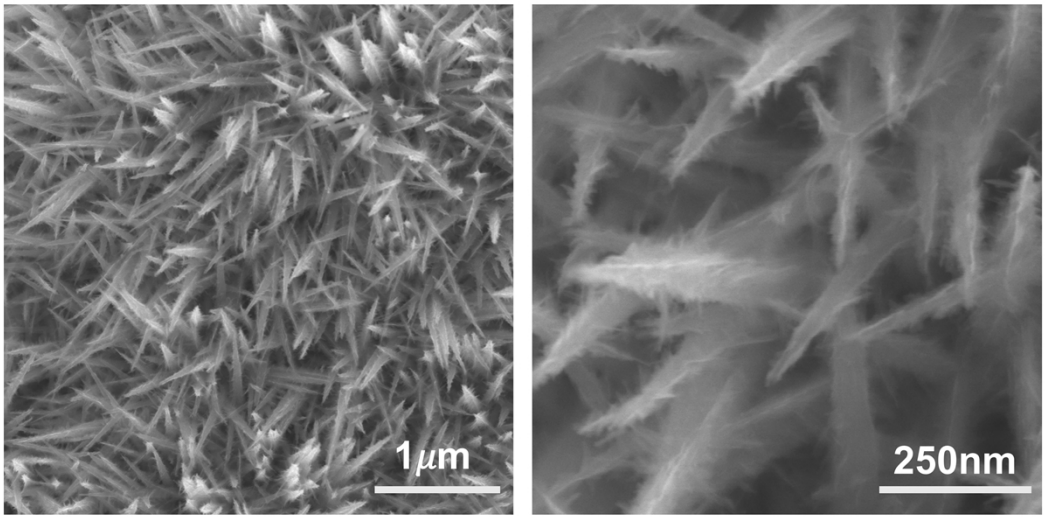

Figure S2. SEM images of α-MnO_2 nanoneedles obtained.

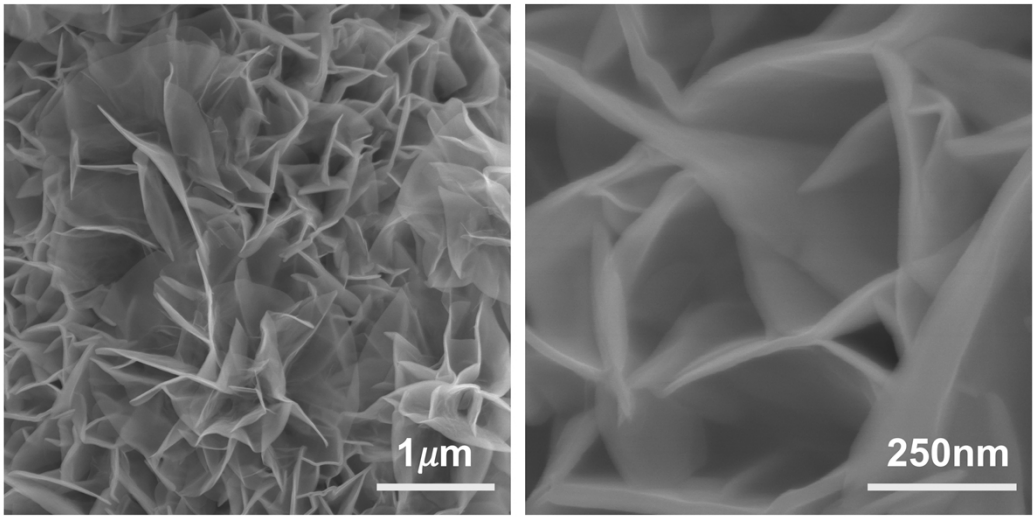

Figure S3. SEM images of α-MnO_2 nanosheet obtained.

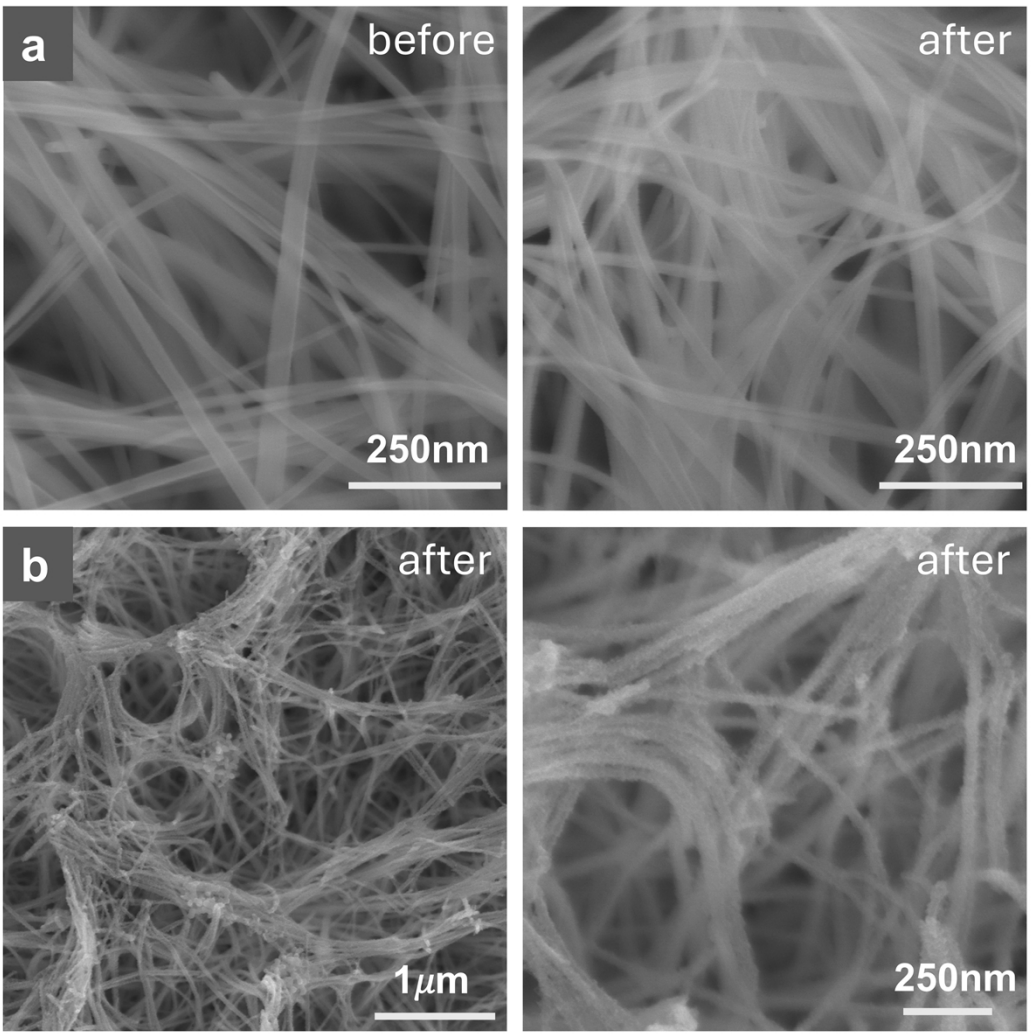

Figure S4. SEM images: (a) MnO_2 NW before and after Ru ion exchange; (b) Ru-MnO_2 NW with different sizes after calcination at 200 ℃.

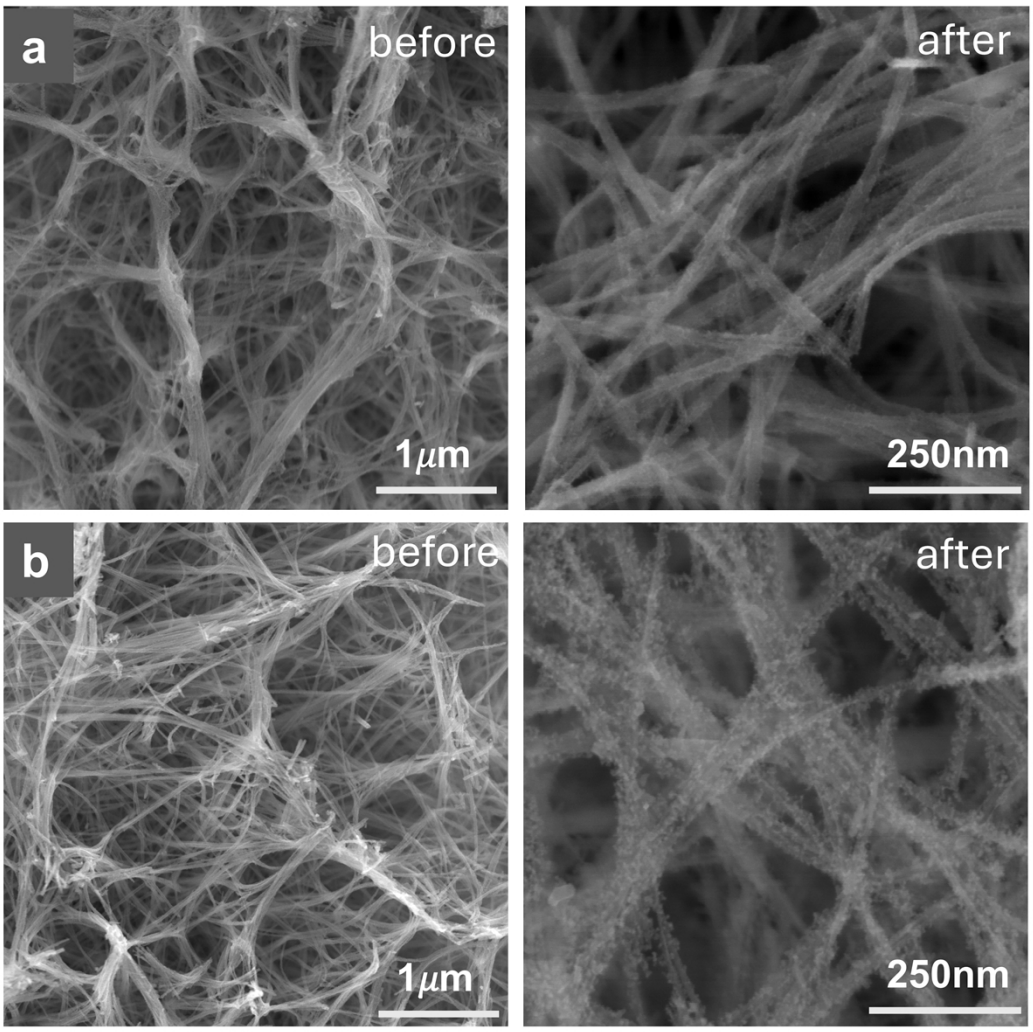

Figure S5. SEM images of Ru-MnO_2 NW before and after calcination at different temperatures: (a) 400 ℃, (b) 600 ℃.

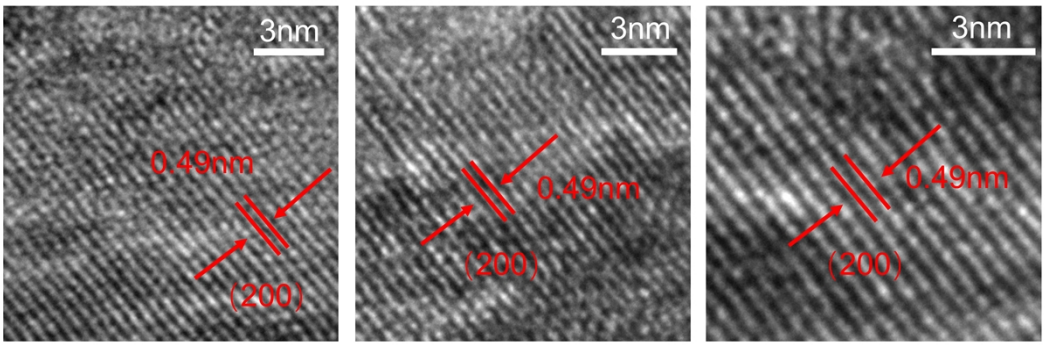

Figure S6. TEM lattice fringes of Ru-MnO_2 NW.

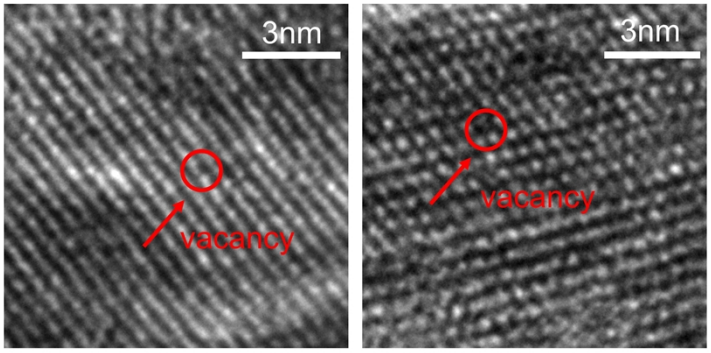

Figure S7. Vacancy defects of Ru-MnO_2 NW observed via TEM.

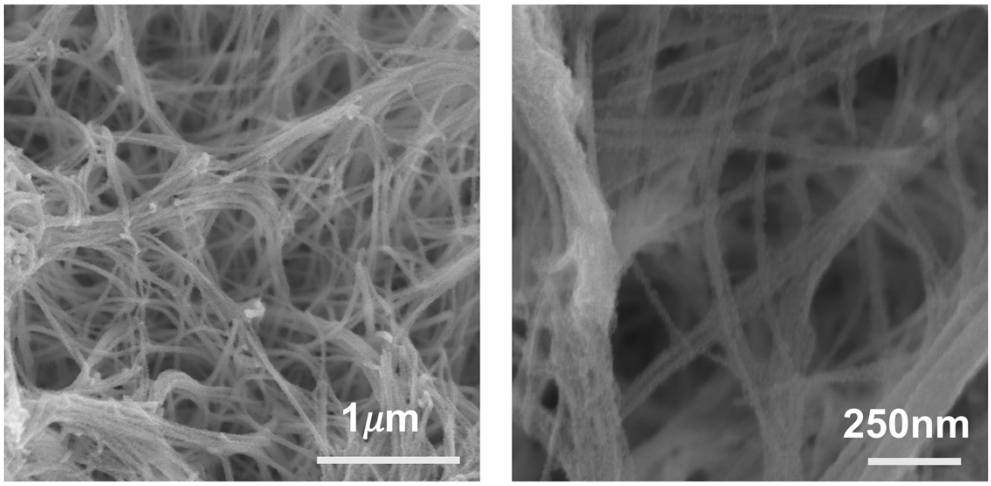

Figure S8. SEM images of Ru MnO_2 NW powder.

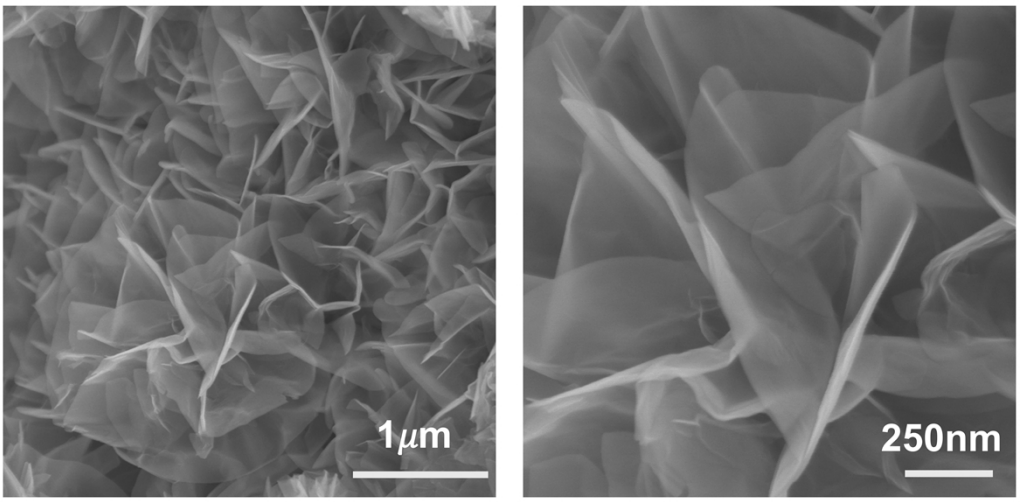

Figure S9. SEM images of Ru MnO_2 NS powder.

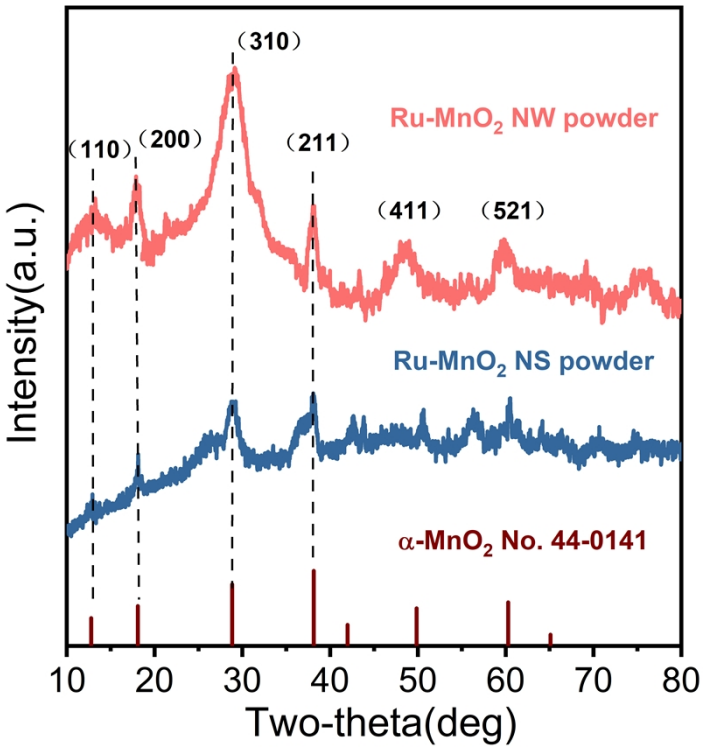

Figure S10. XRD patterns of carbon cloth, Ru–MnO_2 NW powder and Ru–MnO_2 NS powder.

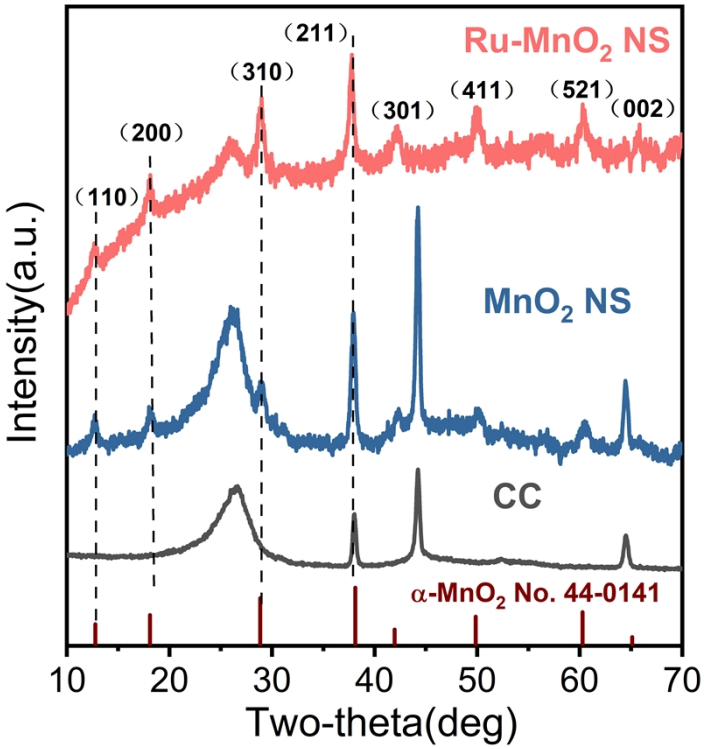

Figure S11. XRD patterns of carbon cloth, MnO_2 NS and Ru–MnO_2 NS, showing retention of the α-MnO_2 phase without detectable crystalline RuO_x.

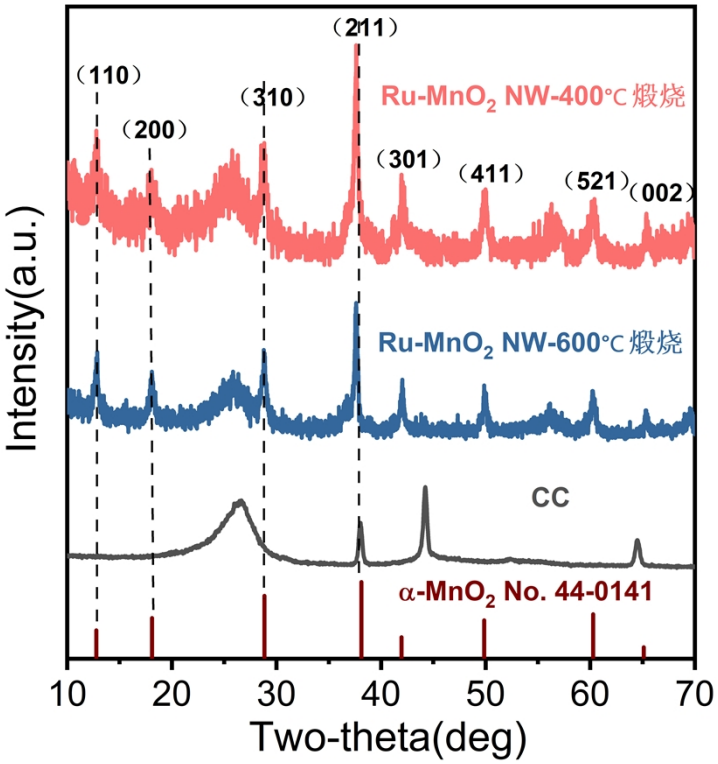

Figure S12. XRD patterns of carbon cloth and Ru–MnO_2 NW calcined at 400 °C and 600 °C.

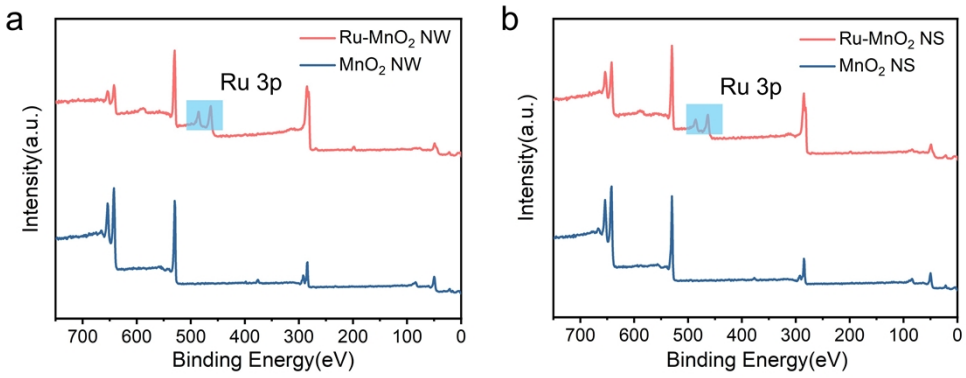

Figure S13. High-resolution XPS full spectrum of (a) Ru-MnO_2 NW and MnO_2 NW, (b) Ru-MnO_2 NS and MnO_2 NS.

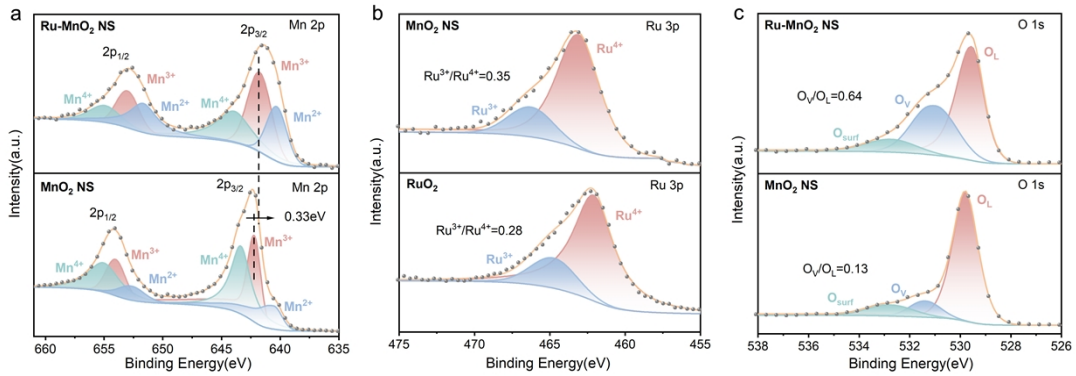

Figure S14. High-resolution XPS spectra of Ru–MnO_2 NS: (a) Mn 2p, (b) Ru 3p and (c) O 1s, evidencing a reduced Mn redox state, an increased vacancy-associated oxygen component, and a higher Ru^{3+}/Ru^{4+} fraction relative to RuO_2.

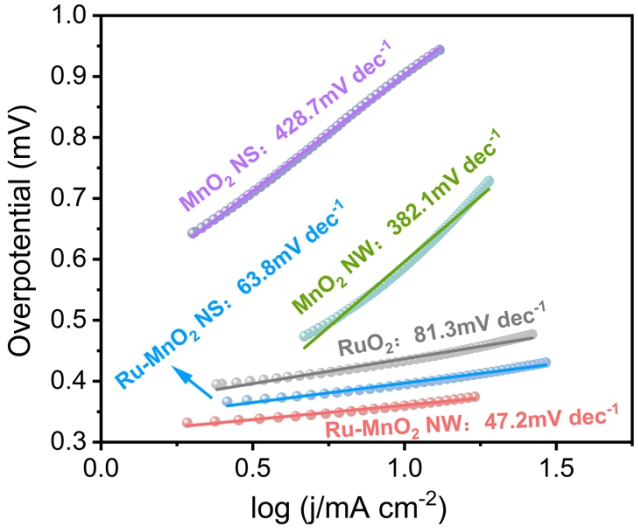

Figure S15. Tafel slope of each sample.

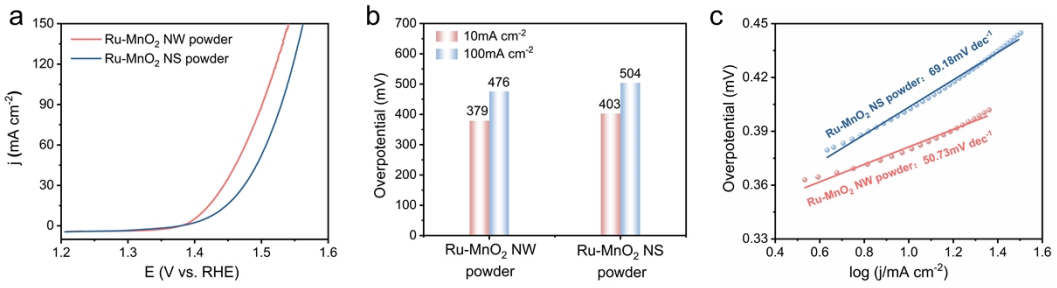

Figure S16. (a) LSV curves of Ru–MnO_2 NW powder and Ru–MnO_2 NS powder in 0.5 M H_2SO_4, (b) Comparison of overpotentials required to reach current densities of 10 and 100 mA cm^{-2}, (c) Corresponding Tafel plots derived from the polarization curves.

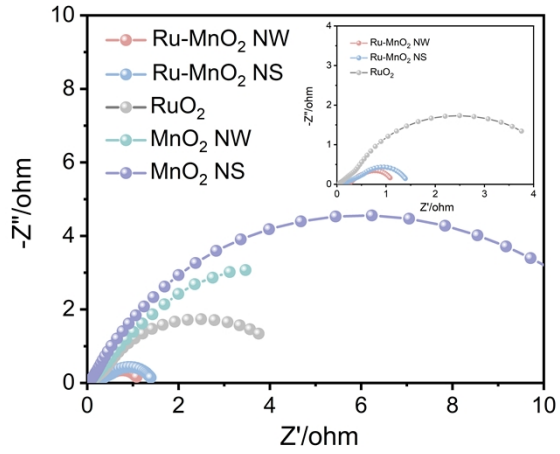

Figure S17. EIS Nyquist plots recorded at 1.4 V_{RHE}.

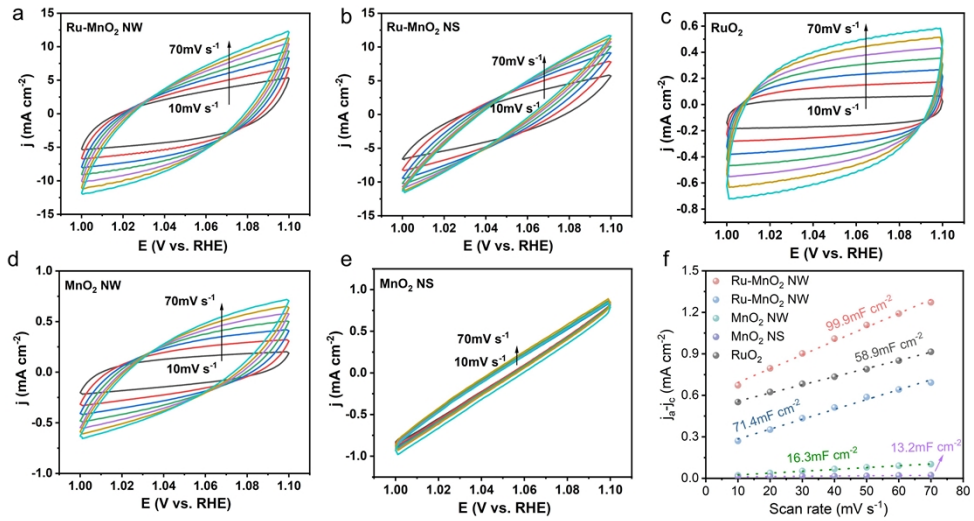

Figure S18. Electrochemical cyclic voltammetry scans recorded for (a) Ru–MnO_2 NW, (b) Ru–MnO_2 NS, (c) commercial RuO_2. (d) MnO_2 NW, (e) MnO_2 NW, (f) Linear fitting of the capacitive currents versus cyclic voltammetry scans for these catalysts.

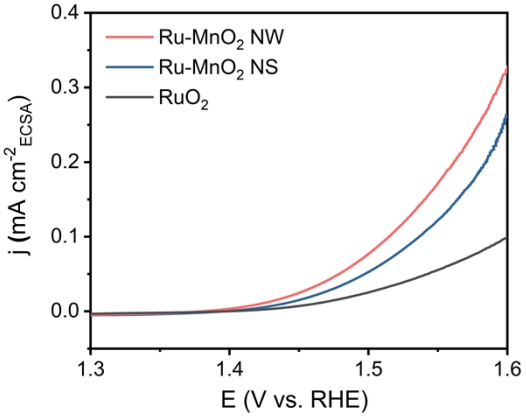

Figure S19. ECSA-normalized OER activities of Ru–MnO_2 NW, Ru–MnO_2 NS and commercial RuO_2.

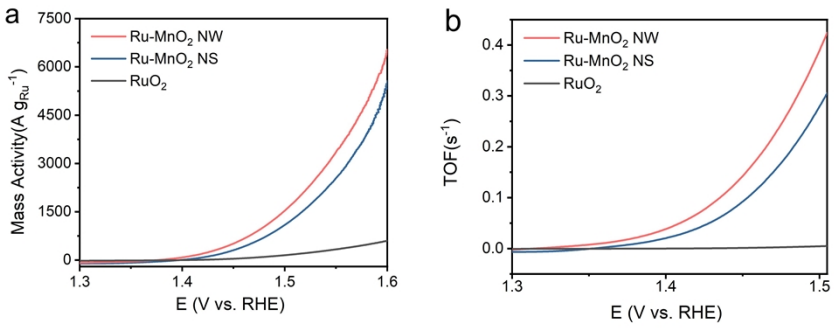

Figure S20. Potential-dependent (a) mass activity and (b) TOF for Ru–MnO_2 NW, Ru–MnO_2 NS and commercial RuO_2.

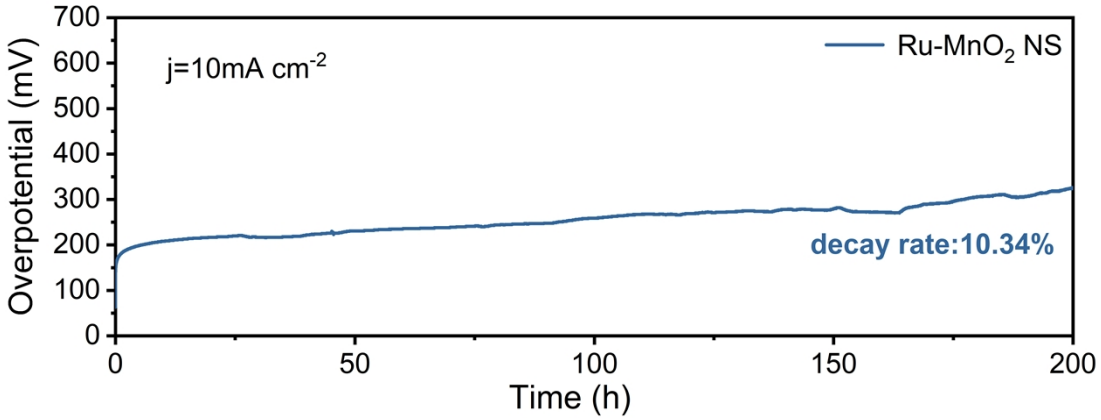

Figure S21. Long-term chrono potentiometric stability test of Ru–MnO_2 NS at a constant current density of 10 mA cm^{-2}.

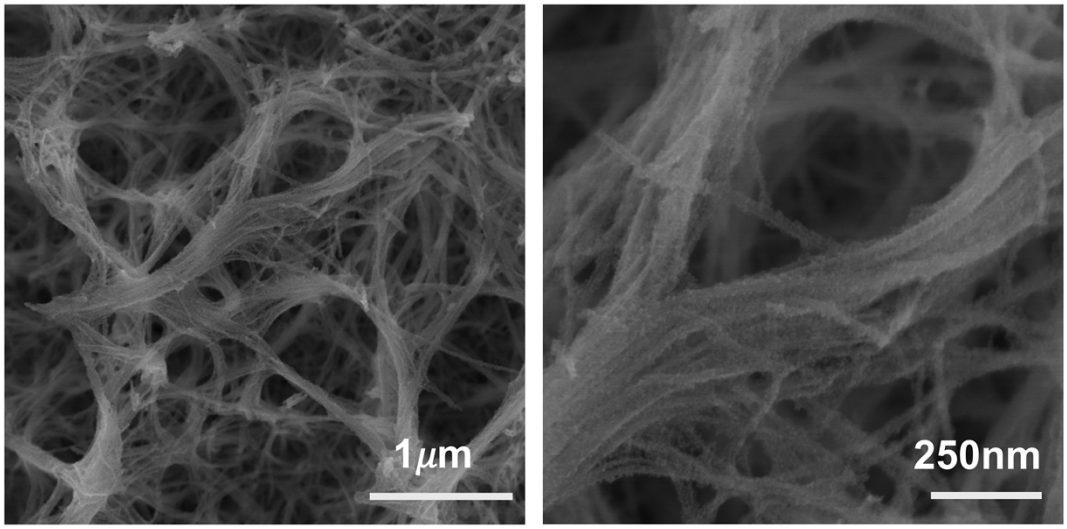

Figure S22. SEM images of Ru-MnO_2 NW after cv.

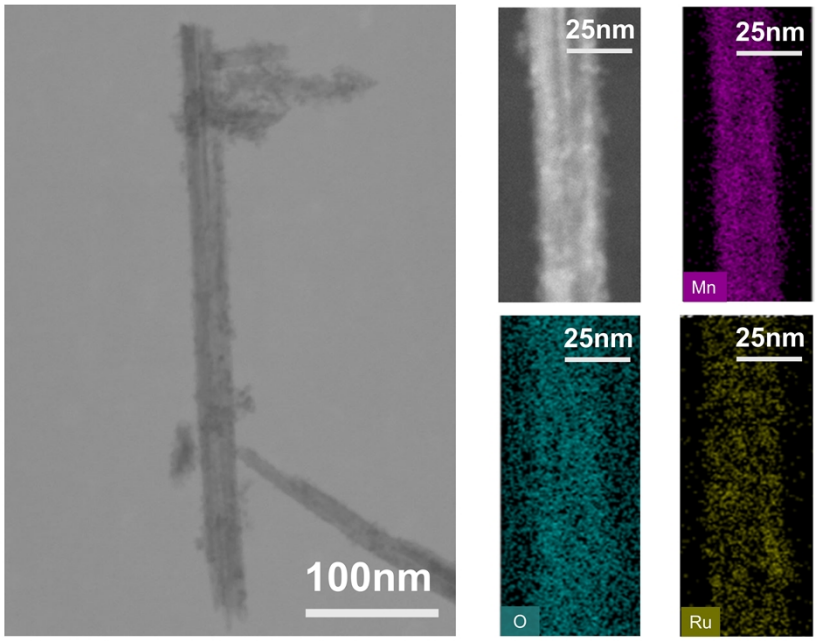

Figure S23. TEM image of Ru–MnO_2 NW after cv and EDS elemental maps of Ru–MnO_2 NW after cv (Mn, O and Ru).

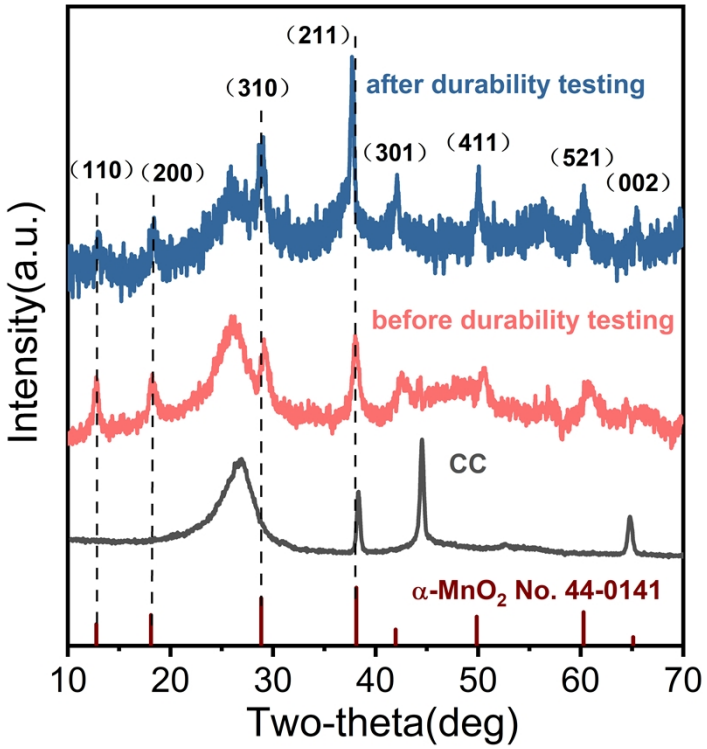

Figure S24. XRD patterns of carbon cloth, Ru–MnO_2 NW and Ru–MnO_2 NW after cv.

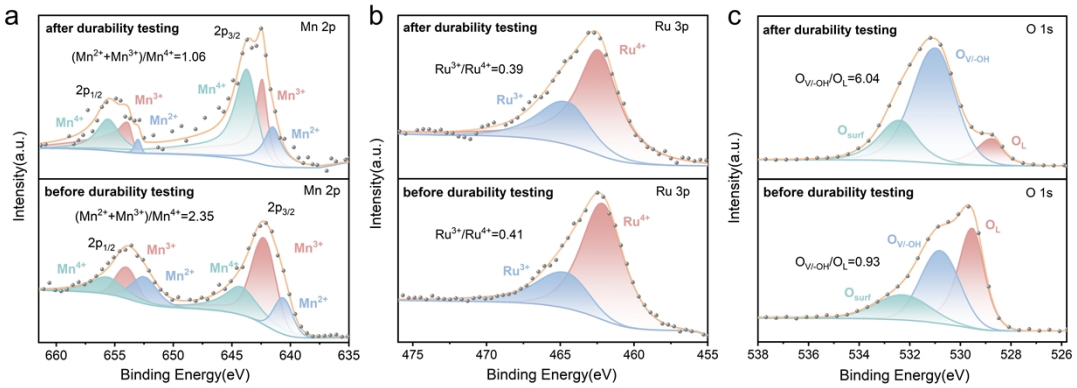

Figure S25. High-resolution XPS spectra of Ru–MnO_2 NW after cv: (a) Mn 2p, (b) Ru 3p and (c) O 1s.

3 Supplementary tables

Table S1. The weight percentage of Ru in Ru-MnO_2 NW and Ru-MnO_2 NS by ICP-OES.

Sample	Ru wt.%
Ru-MnO_2 NW	10.12
Ru-MnO_2 NS	9.96

Table S2. The weight percentage of Ru in Ru-MnO_2 NW powder and Ru-MnO_2 NS powder by ICP-OES.

Sample	Ru wt.%
Ru-MnO_2 NW powder	10.08
Ru-MnO_2 NS powder	9.89

Table S3. Analysis of $(Mn^{2+}+Mn^{3+})/Mn^{4+}$ ratios in all MnO_2 samples based on the high-resolution XPS Mn 2p spectra.

Sample	$(Mn^{2+}+Mn^{3+})/Mn^{4+}$(pristine)
MnO_2 NW	1.07
Ru-MnO_2 NW	2.35
MnO_2 NS	1.43
Ru-MnO_2 NS	2.09

Table S4. Analysis of Ru^{3+}/ Ru^{4+} ratios in all Ru-MnO_2 samples and RuO_2 based on the high-resolution XPS Ru 3p spectra.

Sample	Ru^{3+}/ Ru^{4+}(pristine)
Ru-MnO_2 NW	0.41
Ru-MnO_2 NS	0.35
RuO_2	0.28

Table S5. Analysis of oxygen species in all MnO_2 samples based on the high-resolution XPS O 1s spectra.

Sample	O_L	O_V	O_V/O_L (pristine)	O_{surf}
MnO_2 NW	75.80%	19.59%	0.26	4.61%
Ru-MnO_2 NW	41.35%	38.52%	0.93	20.13%
MnO_2 NS	79.24%	10.17%	0.13	10.59%
Ru-MnO_2 NS	52.92%	33.70%	0.64	13.37%

Table S6. Equivalent-circuit fitting parameters derived from the EIS data.

Sample	R_s (Ω)	R_{ct} (Ω)
Ru-MnO_2 NW	0.90	4.55
Ru-MnO_2 NS	1.17	5.57
RuO_2	1.68	12.50
MnO_2 NW	4.21	32.06
MnO_2 NS	5.73	47.12

Table S7. Comparison of OER performance for Ru-MnO_2 NW and the state-of-the-art electrocatalysts.

Catalyst	Stability (h)	η (mV)	Tafel (mV dec^{-1})	Ref.
Ru-MnO_2 NW	**920**	**179**	**47.2**	**This work**
Sm-Ru_{2-x}-O_V	320	217	45.76	Energy Environ. Sci., 2025, 18, 4276
$RuCoO_x$	100	200	50.1	J. Am. Chem. Soc. 2023, 145, 17995−18006
$Ru_{(anc)}$-Co_3O_4	150	198.5	49.2	J. Am. Chem. Soc. 2023, 145, 23659−23669
$Ru_{(ads)}$-Co_3O_4	12	298.1	128.2	J. Am. Chem. Soc. 2023, 145, 23659−23669
Ru/MnO_2	200	161	29.4	Nat. Catal. 2021, 4, 1012
Ir-MnO_2	650	218	59.6	Joule 2021, 5, 2164
a/c-RuO_2	60	220	48.6	Angew. Chem., Int. Ed. Engl. 2021, 60, 18821
Ru/MnO_2	200	169	29.4	Nat. Catal. 2021, 4, 1012
AD-HN-Ir	100	216	39	Commun. 2021, 12, 6118
Mn-RuIr NCT	180	198	45	Small Methods 2022, 6, 2101236
$W_{0.2}Er_{0.1}Ru_{0.7}O_{2-\delta}$	500	168	66.8	Nat. Commun. 2020, 11, 5368
$SrIrO_3$	1080	196	60	Adv. Mater. 2022, 35, 2208539
$Mn_{7.5}O_{10}Br_3$	500	295	68	Nat. Commun. 2022, 13, 2294
Ru-γ-MnO_2	100	246	57	J. Am. Chem. Soc. 2025, 147, 24392-24402
Ru-β-MnO_2	13	301	61	J. Am. Chem. Soc. 2025, 147, 24392-24402